AIAA 2001-0437
Stable High-Order Schemes and DNS of Boundary-Layer Stability on a Blunt Cone at Mach 8

Xiaolin Zhong and Mahidhar Tatineni
University of California, Los Angeles
Los Angeles, CA

39th Aerospace Sciences Meeting & Exhibit
8-11 January 2001 / Reno, NV

STABLE HIGH-ORDER SCHEMES AND DNS OF BOUNDARY-LAYER STABILITY ON A BLUNT CONE AT MACH 8

Xiaolin Zhong * **and Mahidhar Tatineni** †
University of California, Los Angeles, California 90095

ABSTRACT

The objectives of this paper are two fold: 1) to present new high-order (12th or higher order) explicit and compact finite difference schemes with stable boundary closures for the DNS of transitional or turbulent flows; 2) to present results of numerical simulation of nonlinear boundary layer stability of Mach 7.99 axisymmetric flow over a blunt cone. The first part of this paper presents a way to stabilize high-order finite difference schemes with boundary closures. Current numerical methods used in most practical DNS studies of compressible flows are limited to 6th-order or lower in the interior and 4th-order or lower on the boundary because of the numerical instability of the boundary closure schemes. This paper shows that this numerical instability for high-order schemes based on uniform grids is due to the instability of polynomial interpolation based on uniform grids (the Runge phenomena). It is shown that the instability can be overcome for arbitrarily high-order finite difference schemes with stable boundary closure schemes if the schemes are derived directly on a non-uniform stretched grid. Explicit formulas for computing the coefficients of high-order compact (and explicit) schemes on nonuniform grids are derived. The second part of the paper is motivated by a project of NATO RTO Working Group 10 on Boundary Layer Transition to conduct numerical simulation of nonlinear boundary layer stability for blunt cone at Mach 7.99 corresponding to Stetson's experiment. The emphasis is on the nonlinear second mode instability of the hypersonic boundary layer observed in the experiments. The initial results of the first test case under the isothermal wall condition are presented and compared with the experimental results.

INTRODUCTION

The prediction of laminar-turbulent transition in hypersonic boundary layers is a critical part of the aerodynamic design and control of hypersonic vehicles. Most of our knowledge of hypersonic boundary layer stability is obtained by the linear stability theory (LST) [1]. Mack found that there are higher acoustic instability modes in addition to the first-mode instability waves in supersonic and hypersonic boundary layers. Among them, the second mode becomes the dominant instability for hypersonic boundary layers at Mach numbers larger than about 4. The existence and dominance of the second mode has been observed by experimental studies [2,3].

The objectives of this paper are two fold: 1) to present new high-order (12th or higher order) finite difference schemes with stable boundary closures for the DNS of transitional or turbulent flows; 2) to present results of numerical simulation of nonlinear boundary layer stability of Mach 7.99 axisymmetric flow over a blunt cone. These two parts are briefly discussed below.

Stability of High-Order Boundary Closure Schemes

The first part of this paper presents and analyzes new numerically stable high-order finite difference schemes with boundary closures. We have been working on the the numerical simulation of hypersonic boundary-layer transition by developing high-order accurate numerical methods for direct numerical simulation [4,5], and we have developed and validated a set of fifth and seventh-order shock-fitting schemes for the DNS of practical hypersonic flows over blunt bodies. The use of the shock-fitting method makes it possible to accurately compute the physical bow-shock interactions, and the development of instability waves in the boundary layers. It is necessary to use high-order numerical methods in the simulation in order to resolve all length and time scales in complex wave fields in hypersonic boundary layers.

High-order finite-difference methods have recently received much attention for the DNS of transitional and turbulent flows [6-10]. Finite-difference schemes include both traditional explicit schemes and compact [6] schemes. High-order schemes are required because lower-order schemes do not have an adequate accuracy level to resolve a wide range of spatial and temporal scales in the direct numerical simulation of fluid flows. Most finite difference schemes used in direct numerical simulation are either central difference schemes [6,7] with filtering or upwind high-order schemes [5,11-13].

The orders of accuracy of numerical methods used in practical DNS studies, however, are often limited

*Associate Professor, Mechanical and Aerospace Engineering Department, e-mail: xiaolin@seas.ucla.edu, Associate Fellow AIAA.

†Graduate Student, Student Member AIAA

to 6th-order or lower in the interior and 4th-order or lower on the boundary closure schemes because of the numerical instability of the boundary closure schemes. Most high-order explicit and compact finite schemes are derived on a uniformly spaced grid. The schemes are applied to a nonuniform grid by a coordinate transform from the nonuniform physical coordinates to uniform computational coordinate. The finite difference schemes are applied in the uniform computational coordinates through this transformation. The main limiting factor in the application of high-order schemes is the numerical instability of high-order boundary closure schemes [7,14,15]. For example, difference schemes of fourth order or higher are unstable when they are coupled with high-order boundary schemes using one-sided finite-difference approximations [7,14]. Carpenter et al. [14] showed that for a sixth-order inner compact scheme, only a third-order boundary scheme can be used without introducing instability. This results in globally fourth-order accurate schemes even though the inner scheme is sixth-order accurate. For still higher order schemes, it is necessary to use very lower order boundary closure scheme in order to maintain numerical stability. Consequently, the orders of accuracy of numerical methods used in most practical DNS studies are often limited to 6th-order or lower in the interior and 4th-order or lower on the boundary closure schemes because of the numerical instability of the boundary closure schemes. The overall accuracy of the overall schemes are at most one order higher than the order of the boundary scheme no matter how high the order of the interior scheme.

This paper proposes a simple way to overcome the instability in arbitrarily high-order finite difference schemes with boundary closure schemes. We show that numerical instability on high-order boundary schemes is a result of the use of uniform computational grids in applying high-order schemes. An effective way to overcome the instability in arbitrary high-order finite difference schemes with boundary closure schemes can be achieved by using the high-order schemes directly in a non-uniform stretched grid without coordinate transformation. The coefficients of the high-order schemes are determined based on polynomial interpolation in the physical nonuniform grids. The amount of grid stretching is determined to maintain the stability of the overall schemes. This paper presents explicit formulas for computing the coefficients for arbitrary order explicit and compact schemes in a general non-uniform grid. As a result, the high-order schemes can be easily used in applications by computing the derivative coefficients using these explicit formulas. The use of non-uniform grid approach also has the advantage that it does not require the grid spacing to be smooth. The new high-order (up to 12-th order) schemes have been tested in computing a linear wave equation with oscillation boundary conditions. It is found the high-order schemes are stable and produce much higher degree of accuracy. Work is currently underway to apply them to the full Navier-Stokes equations.

Stetson's Stability Experiments

The second part of the paper is motivated by a project of NATO RTO Working Group 10 on Boundary Layer Transition described in [16]. This paper presents our results on numerical simulation of the nonlinear boundary layer stability for blunt cone at Mach 7.99 corresponding to an stability experiment by Stetson et al. [17]. The numerical simulation of the full nonlinear Navier-Stokes equations are able to take in to account the nonlinear wave interactions, the bow shock effects, the wall curvature effects, and the non-parallel mean flow effects on the stability of the boundary layer. The emphasis of the current study is on the nonlinear second mode instability of the hypersonic boundary layer observed in the experiments. The numerical results on the second mode instability and nonlinear interactions are compared with experimental results. It is hoped that the comparison of nonlinear simulation experimental results will lead to a better understanding of the hypersonic boundary layer instability mechanism. The particular test case studied in this paper is a Mach 7.99 axisymmetric flow over a blunt circular cone with nose radius of 0.15 inch at zero angle of attack. Both steady and unsteady flow fields between the bow shock and the boundary layer are numerically simulated by using a high-order shock-fitting scheme to study the wave generation in the boundary layer.

Stetson et al. [17] carried out boundary layer stability experiments for an axisymmetric blunt cone at Mach 7.99. The half angle of the cone is 7° and the freestream Reynolds number based on the nose radius is about 33,449. The total length of the cone is about 270 nose radius. The experiments measure detailed frequency spectra of the disturbance waves along the body surface. The instability waves were found to be dominated by second mode instability. There are also significant components of harmonics of the second modes. They also found evidence of entropy layer instability in the region outside of the boundary layers for a case of blunt cone with large nose radius. The stability characteristics of the boundary layer flow over the blunt cones corresponding to Stetson's experiments have been extensively studied using the linear stability analysis [18–21]. The linear stability analyses predicted slightly lower frequency of the dominant second mode, but much higher amplification rates than the experimental results at a downstream location of 175 nose radius. It has been speculated that the discrepancy between the linear stability results and the experimental results are due to the fact that there are significant harmonic components at the 175 nose radius station in the experimental results. The harmonics are the result of nonlinear interaction

among the second modes. The nonlinear effects are neglected in a linear stability analysis. Furthermore, the effects of bow shocks and non-parallel boundary layers are neglected in a normal mode stability analysis. The initial receptivity process, which becomes very complex due to hypersonic bow shock interaction [22,23], is not considered in the linear stability analysis.

All these effects can be taken into account in a direct numerical simulation of the full Navier-Stokes equations. So far, no DNS studies have been carried out for the stability of Stetson's cone experiment. This paper reports our initial results in the DNS studies of the nonlinear stability of this particular flow. More complete results and analyses will be presented in future papers.

HIGH-ORDER SCHEMES WITH STABLE BOUNDARY CLOSURE

This sections details the numerical methods, formulas and test cases used in the development and validation of stable high-order finite-difference schemes with stable high-order boundary closure for stretched grids. Existing high order schemes have to reduce order at the boundaries in order to ensure stability. In our new approach, we use a stretching function to cluster grids near the boundary to enable high order closure. The effect of stretching is studied by systematically changing the stretching between a Chebyshev distribution and a uniform distribution.

Basic Ideas

A high-order finite difference scheme is based on a polynomial interpolation of increasing degrees to approximate the derivatives of a function. A compact scheme can be derived by a Hermite polynomial interpolation using both the function values and their derivatives. It is well known (the Runge phenomena) that a high-order polynomial interpolation based on a uniform grid distribution develops oscillations near the boundary of the interpolation domain. Higher order polynomials lead to larger oscillations at the boundary. Because finite difference schemes are based on polynomial interpolation, it is not surprising that a high-order finite difference scheme based on uniform grids will develop instability at the boundary closure schemes. This instability of the high-order schemes is a result of the instability of polynomial interpolation on a uniform grid as shown by the Runge phenomena.

On the other hand, a spectral collocation method using the Chebyshev polynomials is identical to a global high-order finite difference scheme using all grid points directly derived on nonuniform grid points located at the zeros or maximas of the Chebyshev polynomials. The Chebyshev grid spacing is as follows:

$$y = \cos(\pi i/N) \tag{1}$$

where i is grid index, N is total number of grid points, and y is the physical coordinate. Therefore, a Chebyshev spectral collocation method using 101 grid points is a 100th-order finite difference scheme using a grid stretching given by Eq. (1). Such a finite difference scheme is based on a polynomial interpolation based on a nonuniform grid distribution without coordinate transformation. Such interpolation is stable both in the interior and in the boundary points because of the condensation of grid points at the boundary. As a result, a 100th-order or higher finite difference scheme based on Chebyshev grid spacing is numerically stable because of the grid stretching at the boundary in the polynomial interpolations. On the other hand, although they are much superior in numerical accuracy, the spectral methods have the drawback that they are computationally expensive because they are global schemes based on all grid points. Such global accuracy may be an overkill in terms of accuracy. For example, it may not be necessary to use a 200th-order scheme as the spectral collocation method for a 200 points domain, because the truncation errors will lose significance because of computer round-off errors. Another drawback of the spectral method is that the grid spacing given by Eq. (1) leads to a highly stretched grid at the wall. It can be shown that the minimum grid spacing at the wall is $O(1/N^2)$. Such fine grid spacing leads to a very restrictive stability requirement in the time step in the temporal integration of the equations.

Therefore, we propose an intermediate approach to use fixed high-order (up to 10 to 15th order) local schemes, while using grid stretching to ensure the stability of boundary closure schemes. At the same time, because the order of the schemes is fixed, the grid stretching at the wall does not need to be as strict as the spectral stretching given by Eq. (1). The minimum grid spacing at the wall can be determined so that the high-order schemes are stable with boundary closure. It can be in the order $O(1/N)$ instead of $O(1/N^2)$.

The application of high-order schemes in non-uniform grids do not introduce additional computational difficulty, while the schemes developed for uniform grids do so. The coefficients of the high-order schemes at each grid point are different because of grid stretching, but they can be computed and saved in memory once and for all at the beginning of a calculation. The conventional methods for deriving the coefficients for the finite difference (especially the compact) schemes is to use the method of undetermined coefficients with Taylor expansions. The coefficients are computed by solving a linear equation for the coefficients. Such methods are not convenient for deriving the coefficients with nonuniform grids because every case may have a different grid spacing. In addition, the matrix in solving the coefficients has high condition numbers, which can lead to large round off errors in solving the linear equations for the coefficients of the high-order schemes.

In this subsection, we present explicit formulas for

computing the coefficients of the explicit and compact higher order schemes for an arbitrary nonuniform grid distribution. Such explicit formulas can be easily used to calculate the coefficients of high-order schemes for discretizations. A general purpose FORTRAN subroutine has been written to calculate the coefficients for both explicit and compact schemes on nonuniform grid and is available upon requests to the authors by e-mail.

Explicit Scheme Coefficients in Nonuniform Grid

The derivation for the coefficients for the explicit high order schemes on nonuniform grids is straight forward. They are listed here for completeness. The coefficients are derived from a Lagrange polynomial interpolation. For the case of N grid stencil with arbitrary distribution of grid points with coordinates x_i, the $N-1$ degree interpolation polynomial is:

$$P_n(x) = \sum_{j=1}^{N} l_j(x)\, u_j \tag{2}$$

where u_j is the variables at the node points, and

$$l_j(x) = \prod_{l=1, l\neq j}^{n} (x - x_l) \;/\; \prod_{l=1, l\neq j}^{n} (x_j - x_l) \tag{3}$$

The derivative at a grid point x_i can be calculated by differentiating the above polynomial as:

$$u_i' = \sum_{j=1}^{N} b_{i,j}\, u_j \tag{4}$$

where the coefficients $b_{i,j}$ in the derivatives are different for different grid point with index i, and are given by

$$b_{i,j} = l_j'(x_i) \tag{5}$$

and $l_j'(x_i)$ is calculated as follows:

If $i \neq j$:

$$l_j'(x_i) = \prod_{l=1, l\neq j, l\neq i}^{n} (x_i - x_l)/a_j \tag{6}$$

If $i = j$:

$$l_j'(x_i) = \sum_{i=1, i\neq j}^{n} \left(\prod_{l=1, l\neq j, l\neq i}^{n} (x_i - x_l)/a_j \right) \tag{7}$$

where a_j is :

$$a_j = \prod_{l=1, l\neq j}^{n} (x_j - x_l) \tag{8}$$

Hence, once the x_i locations of the stencil are known the coefficients for the finite difference formulas for a high-order scheme in a nonuniform grid can be calculated explicitly using the above formulas. The coefficients at the boundary closure scheme are derived using the same formula by specifying one-sided grid stencils. The derivatives at all grid points, including the interior and boundary points, can be combined into the following vector formula:

$$\boldsymbol{u'} = \boldsymbol{A}\boldsymbol{u} \tag{9}$$

where $\boldsymbol{u}$ is a vector of variables and $\boldsymbol{A}$ is a banded coefficients matrix, which can be computed once and for all at the beginning of a calculation.

The truncation error of the polynomial interpolation is as follows:

$$f(x) - P_n(x) = \frac{f^{n+1}(\xi)}{(n+1)!}(x - x_0)(x - x_1)...(x - x_n) \tag{10}$$

Compact Scheme Coefficients in Nonuniform Grid

In this paper, the explicit formulas for computing the coefficients of a compact schemes in arbitrary nonuniform grids is derived based on a generalized Hermite interpolation polynomial. Consider a generalized Hermite polynomial interpolation to compute u_0' by interpolation through two groups of grid points: 1) interpolates through both u_i and u_i' for n grid points located at x_i for $(i = 1, \cdots n)$, and 2) interpolates through only u_i for additional $m+1$ grid points located at x_j for $(j = 0, -1, \cdots - m)$. An example of the grid stencil is shown in Fig. 1 for a 7-3 compact scheme on a nonuniform grid. The locations of these node points do not have to be arranged in a particular order, as long as they are distinct points.

The generalized Hermite interpolation polynomial is:

$$\overline{H}(x) = H_n(x) + \sum_{j=0}^{-m} \phi_j(x) d_j \tag{11}$$

$H_n(x)$ is the Hermite interpolant for the first group of n grid points without x_0 :

$$H_n(x) = \sum_{i=1}^{n} u_i h_i(x) + \sum_{i=1}^{n} u_i' \widetilde{h}_i(x) \tag{12}$$

where :

$$h_i(x) = [1 - 2l_i'(x_i)(x - x_i)]\, l_i^2(x) \tag{13}$$

$$\widetilde{h}_i(x) = (x - x_i) l_i^2(x) \tag{14}$$

The function $\phi_j(x)$ is defined as:

$$\phi_j(x) = (\xi_j(x))^2 l_j(x) \tag{15}$$

where:

$$\xi_j(x) = \prod_{l=1}^{n} \frac{x - x_l}{x_j - x_l} \tag{16}$$

The values of d_j are determined so that the polynomial interpolates through the second group of $m+1$ grid points (including x_0). There are $m+1$ conditions for solving for d_j:

$$\overline{H}(x_j) = u_j, \qquad j = 0, -1, ..., -m \tag{17}$$

The d_j values are substituted back into the original interpolation polynomial. The formula for the compact derivatives can be derived by evaluating

$$u'_0 = \overline{H}'_n(x_0) \tag{18}$$

This formula leads to the compact coefficients as follows:

$$\sum_{i=0}^{n} b_i u'_i = \sum_{i=0}^{n} a_i u_i + \sum_{j=0}^{-m} c_j u_j \tag{19}$$

where the coefficients a_i, b_i, and c_j are determined by

$$b_0 = 1 \tag{20}$$

$$b_i = -\left[\widetilde{h}_i{}'(x_0) - \sum_{j=0}^{-m} \widetilde{h}_i(x_j)\phi'_j(x_0)\right] \tag{21}$$

$$a_i = +\left[h'_i(x_0) - \sum_{j=0}^{-m} h_i(x_j)\phi'_j(x_0)\right] \tag{22}$$

$$c_j = \phi'_j(x_0) \tag{23}$$

It is easy to test that the formulas above lead to the same compact scheme formulas on a uniform grid. For example, a 6th-order compact scheme can be derived using the above formulas with a 5-3 stencil as follows:

$$20\, u'_{i-1} + 60\, u'_i + 20\, u'_{i+1} = \frac{1}{h}\sum_{k=-2}^{2} a_{i+k}\, u_{i+k} \tag{24}$$

where $a_{i\pm2} = \pm\frac{5}{3}$, $a_{i\pm1} = \pm\frac{140}{3}$, and $a_i = 0$.

Hence, given the grid distribution, the compact scheme coefficients can be calculated explicitly without using the Taylor expansion for uniform or nonuniform grids. The coefficients at the boundary closure scheme are derived using the same formula by specifying one-sided grid stencils. Similarly, the derivatives at all grid points, including the interior and boundary points, can be combined into the following vector formula:

$$\boldsymbol{P}\boldsymbol{u}' = \boldsymbol{Q}\boldsymbol{u} \tag{25}$$

where $\boldsymbol{P}$ and $\boldsymbol{Q}$ are banded coefficients matrices, which can be computed once and for all at the beginning of a calculation. In the stability analysis, the compact scheme can also be written into explicit form as

$$\boldsymbol{u}' = \boldsymbol{A}\boldsymbol{u} \tag{26}$$

where $\boldsymbol{A} = \boldsymbol{P}^{-1}\boldsymbol{Q}$.

Examples of these coefficients matrix for high-order compact schemes on non-uniform grids are shown in the Appendix. Once the coefficients are computed, the higher-order explicit or compact schemes can be used to discretize a first-order derivative in numerical simulation by using the formulas given by Eqs. (9) or (25). The matrix multiplication is only partially carried because $\boldsymbol{P}$ and $\boldsymbol{Q}$ are banded matrices.

Similar explicit formulas for second derivatives can also be derived by a generalized Hermite interpolation formula. They are not presented here.

Grid Spacing

The stability of high-order schemes is dependent on the grid clustering near the boundaries. Spectral collocation methods utilizing the Chebyshev spacing are stable for arbitrary order schemes with boundary closure. The Chebyshev grid spacing is given by Eq. (1). However, this spacing is very restrictive on the timestep ($O(1/N^2)$) in a temporal integration of a PDE. In this paper we are using a less restrictive spacing with high-order finite difference schemes in order to maintain stability and high spatial accuracy and an $O(1/N)$ in minimum grid spacing and timestep.

In this paper, the grid spacing in the numerical simulations is controlled using the stretching function proposed by Kosloff and Tal-Ezer [24] for a spectral method, i.e.,

$$x = \frac{\sin^{-1}(-\alpha\cos(\pi i/N))}{\sin^{-1}\alpha} \tag{27}$$

where the parameter α is used to change the stretching of the grid points from one limit of a Chebyshev grid at $\alpha \to 0$ and the other limit of an uniform grid at α=1. Figure 2 shows a x vs. i/N plot for the stretching function (N=101). A grid stretching factor can be measured by $\Delta x_{min}/\Delta x_{uniform}$, where Δx_{min} is the minimum grid spacing in the stretching grid and $\Delta x_{uniform}$ is the average grid spacing. Figure 3 shows the grid stretching factor as a function of the stretching parameter α (for N=51). Hence, the stretching can be controlled to find the optimum α for which the high order scheme is stable.

Asymptotic Stability Analysis

The asymptotic stability of the high-order explicit and compact schemes with boundary closures is analyzed by computing the eigenvalues of the matrices obtained by spatial discretization of the following wave equation

$$\frac{\partial u}{\partial t} + c\frac{\partial u}{\partial x} = 0 \tag{28}$$

in a fixed computational domain $(-1, 1)$. The non-periodic boundary condition is specified at $x = -1$ to

a fixed value $u(x = 1, t) = f(t)$. After a computational grid has been assigned to the domain, the spatial derivatives of all grid points, including the interior and boundary points, are discretized by a explicit or compact finite difference algorithms given by Eqs. (9) or (25). Substituting the approximation above into the wave equation (28) with the non-periodic boundary condition at $x = -1$ leads to

$$\frac{d\boldsymbol{u}}{dt} = c\boldsymbol{M}\boldsymbol{u} + \mathrm{g}(t) \tag{29}$$

The asymptotic stability condition for the semi-discrete equations is that all eigenvalues of matrix $\boldsymbol{M}$ contains no positive real parts.

The asymptotic stability, which requires that the eigenvalues of the spatial discretization matrices contain no positive real parts, is necessary for the stability of long-time integration of the equation. The eigenvalue analysis is a necessary condition for the stability of the schemes when the matrices do not have full sets of eigenvalues and eigenfunctions. Numerical computations show that the matrices for high-order upwind schemes with boundary conditions have full eigenvalues. For such normal matrices, the eigenvalue analysis is accurate in assessing the stability of high-order finite-difference schemes.

Figure 4 shows the spectrum for a 6th-order scheme on a uniform grid of 101 points. The grid stencil in the interior is to use seven points to evaluate the derivative at the center node point, and use one-sided seven point stencil as boundary closure scheme. The figure shows there are two eigenvalues in the unstable region of the spectrum. Therefore a 4th-order scheme with boundary closure will not be stable because a uniform grid is used.

In order to stabilize the 6th-order scheme, a stretched grid given by Eq. (27) is used for the seven stencil scheme in the physical domain. It is found that the stability of the scheme improve as the grid becomes more and more stretched towards the boundary by decreasing the value of α. Figures 5 and 6 show the spectrum for the 6th-order scheme on a stretched grid with $\alpha = 0.9997$ and $\alpha = 0.9995$ respectively. The two unstable eigenvalues become less unstable for $\alpha = 0.9997$ and are completely stable for $\alpha = 0.9995$. Hence, computing the derivatives directly on a stretched grid results in a stable boundary closure.

It is also found that as the order increases, the amount of grid stretching needs to be increased in order to stabilize the schemes with boundary closure. Therefore, it is necessary to determine the grid stretching needed for stable algorithms as a function of the order of the finite difference algorithm and the number of total grid points in the domain. The stability results for the 4th, 6th, 8th, 10th, and 12th order schemes are presented in Fig. 7. The minimum Δx_{min} required for a stable closure is plotted versus the total number of points, for all schemes. The Δx_{min} is normalized by averaged grid spacing $\Delta x_{uniform} = 2/N$. The results show that higher-order schemes required smaller Δx_{min} in order to maintain stable boundary closure. As N increases, the value of $\Delta x_{min}/\Delta x_{uniform}$ approach a constant value, which means that the required minimum grid spacing is in the order of $1/N$. Hence, the high order schemes are less restrictive than spectral methods (where the Δx_{min} is of order $1/N^2$).

The variation of minimum required grid spacing Δx_{min} for stability with the order of accuracy (stencil width) is shown in Fig. 8. The figure shows that for 6th to 20th order schemes Δx_{min} is approximately of $\mathrm{O}(1/(NM))$ for a finite difference scheme using a set of local stencil width of M ($M - 1$-th order scheme). This is much less restrictive than the $\mathrm{O}(1/N^2)$ spacing in the case of the spectral collocation method based on Chebyshev polynomial.

As stated earlier, the instability of the boundary closure scheme is a result of oscillation of polynomial interpolation at the boundary on a uniform grid. It is can also be demonstrated by the distribution in the interpolation error formula given by Eq. (10), where the error is proportional to the following function:

$$g(x) = (x - x_0)(x - x_1)...(x - x_n) \tag{30}$$

The error in approximating the derivative at a grid points x_i is given by $g'(x_0)$.

Figure 9 shows the distribution of the truncation error for a 11 points global scheme with three different grid spacing: 1) uniform grid, 2) stretching grid, and 3) spectral collocation grid. The figure clearly shows that the use of uniform grid produces large error at the boundary, while the use of stretching grid produces relatively uniform errors in the whole domain. The error at the boundary for uniform grid increase rapidly as the order of the schemes increase. Figure 10 shows the distribution of the error function given by Eq. (30) (normalized by the maximum uniform grid truncation error) for a sixth order scheme on a Chebyshev spacing and two intermediate stretching cases. The truncation error is oscillatory near the boundary for the intermediate stretching cases. This is clearly seen in Fig. 11 which is a zoomed version of Fig. 10. When the stretching is moved closer to the uniform case the oscillations are larger in magnitude which can result in an unstable scheme. Hence, for a stable closure the truncation error near the boundaries must be kept low.

The stability analysis was repeated with compact schemes with similar results. We tested four cases of compact schemes with a 5-3 (7th order), 7-3 (9th order), 7-5 (11th order), and 9-3 (12th order) grid stencil. An example of the derivative matrix of the 7-3 compact scheme with 15 grid points is shown in the Appendix for the stretching grid of $\alpha = 0.8$. Figure 12 shows the eigenvalue spectrum for a $7 - 3$ compact scheme on a uniform grid. The scheme is clearly unstable if high order accuracy is retained at the boundary. Figure 14

shows the same scheme on a nonuniform grid ($\alpha = 0.8$ in the stretching function). The scheme is now stable and has high order boundary closure. Hence, for both explicit and compact high order schemes, clustering grids near the boundaries stabilizes the schemes and allows high order accuracy without the timestep restrictions encountered in spectral methods.

The stability for other compact schemes of higher order have also been evaluated. The variation of minimum required grid spacing Δx_{min} for stability with the high-order compact schemes is shown in Fig. 13. The figure shows that for up to 11th-order, the compact schemes can be stabilized by requiring Δx_{min} to be smaller than a certain number, however, the 12th-order cannot be stabilized when the grids are stretched. The reason is not clear at this point. The results indicated that the compact schemes of very high order is not stable with boundary closure. Therefore, only moderately high order compact schemes (up to 11th order) can be used with grid stretching. On the other hand, there is not stability problem for arbitrarily high-order explicit finite difference schemes, as long as the grid stretching is below the limits shown in Fig. 8.

Results of Wave Equation Computations

The high order explicit and compact schemes are tested by solving the one-dimensional linear wave equation. Work is underway to test the algorithm for the Navier-Stokes equations. The main objective of the tests are to evaluate the accuracy of using very high-order schemes and their numerical stability.

The model equation used is given by Eq. (28). The non-periodic boundary condition is set at the left boundary as

$$u(-1,t) = \sin(\omega \pi t) \qquad t \geq 0 \quad (31)$$

The wave equation is solved in a fixed computational domain $(-1, 1)$. The parameters of the calculations are: $c = 1$, $\omega = 1$. The computations are performed for the 2nd, 4th, 6th, 8th, 10th, and 12th order explicit schemes on the same stretched grid with the stretching parameter $\alpha = 0.91$. The boundary closure scheme is the same order as the interior so that there is no loss of accuracy due to boundary schemes. This grid stretching parameter satisfies the stability condition for all these schemes. The calculations are done using 21, 41, 51, and 101 grids. The time stepping scheme is a Runge-Kutta 4th-order scheme, where the time step is chosen and tested to be small enough so that the temporal errors are smaller than spatial errors.

As expected, the computations of all orders are stable with high-order boundary closure schemes. Figure 15 shows a typical result on the comparison for 6th order scheme on a stretched grid with the stretching parameter $\alpha = 0.91$. The boundary closure is now stable and there is excellent agreement between the numerical and exact solutions. The error distribution for the 10th order scheme is shown in Fig. 16. The average error for all the schemes and grid sizes are shown in Table 2. The results show the advantage of using higher order schemes. The errors of the results using 21 grid points reduced substantially when the order of the schemes increases. The error of a second order scheme is 0.3E-01 using 21 points. The error reduced to 0.6E-09 for the 12th-order scheme. The stretching allows high order accuracy and stability to be maintained at the boundary.

On the other hand, the computation of a 4th-order or higher schemes are not stable if the grid is uniform. Figure 17 shows a typical result of the comparison of the numerical solution with the exact solution for a 6th order interior and boundary scheme on a uniform grid at $t = 2.2$ seconds. The instability at the boundary can be seen. This instability will develop rapidly to lead to a diverged numerical solution at later time steps. The use of a stretched grid, but computed by a high-order scheme derived on a uniform computational coordinates through a coordinate transformation also leads to numerical instability at the boundary. Figure 18 shows the comparison of numerical solution (at $t = 0.01s$) using the stretched grid computed by a 6th order explicit scheme on a uniform grid through coordinate transformation. The computations develop numerical instability at the boundary and will diverge at a later time. Hence, using a uniform grid distribution with high orders leads to an unstable scheme. As detailed earlier, the new scheme is stable with high order boundary closure.

STABILITY OF MACH 7.99 FLOW OVER A BLUNT CONE

Governing Equations and Numerical Methods

The stability of axisymmetric laminar hypersonic flow over a blunt cone at zero angle of attack is computed using a three-dimensional grid. The governing equations are briefly presented in this section. Details can be found in previous papers for 2-D and 3-D flows [4,25]. The governing equations are the unsteady full three-dimensional Navier-Stokes equations written for the computation in the conservation-law form:

$$\frac{\partial U^*}{\partial t^*} + \frac{\partial F^*{}_j}{\partial x_j^*} + \frac{\partial F^*{}_{vj}}{\partial x_j^*} = 0 \qquad (32)$$

where superscript "$*$" represents dimensional variables, and

$$U^* = \{\rho^*,\ \rho^* u_1^*,\ \rho^* u_2^*,\ \rho^* u_3^*,\ e^*\}. \qquad (33)$$

The gas is assumed to be thermally and calorically perfect. The viscosity and heat conductivity coefficients are calculated using Sutherland's law together with a constant Prandtl number, Pr. The equations are transformed into body-fitted curvilinear computational coordinates in a computational domain bounded by the bow

shock and the body surface. The location and the movement of the bow shock is an unknown to be solved with the flow variables by a shock-fitting method.

The numerical simulation for the axisymmetric hypersonic flow over a blunt cone is carried out using our 3-D fifth-order shock fitting scheme where the outer grid line is the bow shock. The unsteady bow shock shape and shock oscillations are solved as part of the computational solution. The numerical methods for spatial discretization of the 3-D full Navier-Stokes equations are a fifth-order shock-fitting scheme in streamwise and wall-normal directions, and a Fourier collocation method in the periodic spanwise flow direction for the case of a wedge geometry or in the azimuthal direction for the case of a cone geometry. The spatially discretized equations are advanced in time using a Runge-Kutta scheme of up to third order.

Because the flow field behind the bow shock is not uniform, the flow variables are nondimensionalized using the freestream conditions as characteristic variables. Specifically, we nondimensionalize the velocities with respect to the freestream velocity U^*_∞, length scales with respect to a reference length d^*, density with respect to ρ^*_∞, pressure with respect to p^*_∞, temperature with respect to T^*_∞, time with respect to d^*/U^*_∞, vorticity with respect to U^*_∞/d^*, entropy with respect to c^*_p, wave number by $1/d^*$, etc. The dimensionless flow variables are denoted by the same dimensional notation but without the superscript "$*$".

Flow Conditions

The flow conditions are the same as Stetson's experiments. Specifically,

$M_\infty = 7.99$
$p^*_t = 4 \times 10^6\ Pa$ $\qquad T^*_t = 750\ K$
$\gamma = 1.4$ $\qquad Pr = 0.72$
$Re_\infty = \rho^*_\infty U^*_\infty r^*_n/\mu^*_\infty = 33,449$

The viscosity is computed using the Sutherland's law for air. The cone is a 7° half angle blunt cone with spherical nose of radius: $r^*_n = 3.81 \times 10^{-3}\ m$. The total length of the cone is $L = 1.016\ m$. The body surface is assumed to be a non-slip wall with either an isothermal wall with temperature T^*_w or an adiabatic wall.

The wall temperature in the experiment was neither isothermal nor adiabatic. In order to access the effects of wall temperatures on the boundary-layer stability properties, a number of cases with different isothermal wall temperatures and a case of adiabatic wall are considered. So far, we have finished the first case of higher wall temperature of $T^*_w = 800\ K$ and are currently computing the case with adiabatic wall. The results presented in this paper is mainly for the case of isothermal wall with $T^*_w = 800\ K$. Whenever possible, the numerical solutions are compared with the experimental results published by Stetson et al. [17] and some newly compiled results by Schneider [16].

The main objective of this paper is to study the nonlinear stability of the second modes and harmonics. In stability experiments of Stetson et al. [17], the instability waves in the boundary layer were generated naturally in a relatively noisy wind tunnel without artificial forcing disturbances. Stetson et al. [17] showed detailed frequency spectra of disturbance waves at various surface stations. The wave spectra show clearly that the instability waves are dominated by two-dimensional second modes and their harmonics. As the observation stations move downstream, the frequency of the dominant second mode reduces and the strength of the harmonics increases. At the station of 175 nose radius, the second mode waves is maximum at the frequency of about 135 kHz.

In order to reproduce similar flow conditions in the numerical simulations, it is necessary to introduce initial forcing waves to excite the instability waves in the boundary layer. The forcing waves can originate from the freestream or at the wall by surface roughness or vibrations. It is a difficult task to simulate a stability experiment without knowing exactly the source of the initial disturbances. As a first step in our numerical simulation, we introduce the disturbances by the blowing and suction of a narrow surface strip in the upstream region of the body surface. Since the wave fields in the experiment contain a wide range of second-mode frequencies, we introduce, by surface blowing and suction, disturbances of a number of frequencies near the dominant second mode waves in the simulation. The subsequent receptivity and development of the instability waves at these frequencies and their harmonics due to nonlinear interactions are computed by the numerical simulation.

The specific formula for surface blowing and suction in a narrow upstream range are given by the perturbations to the wall normal velocity, i.e.,

$$\begin{aligned} v_n(x,t) &= \epsilon \sin[\alpha_w(x-x_0)] \\ &\quad \sum_{k=k_0}^{k=k_1} A_k \cos(k\omega_0 t + \phi_k) \qquad (34) \\ &\quad (x_0 \le x \le x_1) \end{aligned}$$

where ϵ is a small nondimensional number representing forcing disturbance amplitudes. The forcing disturbances contain a number of wave frequencies which are multiples of ω_0, which are chosen such that the frequencies cover the dominant second-mode frequencies observed in the experiment. The amplitudes of the forcing waves can be changed by varying the value of ϵ to study the nonlinear wave interactions. The forcing frequency ω^* is commonly represented by a dimensionless frequency F defined by

$$F = 10^6\ \frac{\omega^* \nu^*}{U^{*2}_\infty} = 10^6\ \omega/Re_\infty\ . \qquad (35)$$

The numerical simulation for an unsteady hypersonic layer stability problem is carried out in two steps. First, a steady flow field is computed by advancing the unsteady flow solutions to convergence with no disturbances imposed. Second, unsteady viscous flows are computed by imposing blowing-and-suction, at the narrow surface strip, on the steady flow variables according to Eq. (34). In the first test case, the blowing and suction strip is located at about 135 nose radius surface station, with seven discrete wave modes of different frequencies of the same forcing amplitudes.

Table 1: Frequencies introduced by surface blowing and suction.

k	Frequency $\frac{k\omega_0}{2\pi}$ (kHz)	F
9	89.53	240.1
10	99.48	266.8
11	109.4	293.5
12	119.4	320.2
13	129.3	346.8
14	139.3	373.5
15	149.2	400.2

Steady Base Flow Solutions

The steady base flow solutions of the Navier-Stokes equations for the axisymmetric Mach 7.99 flow over the blunt cone are obtained first by advancing the solutions to a steady state without freestream perturbations. The simulation is carried out using a multi-zone approach using 21 zones with a total of 1260 by 121 grid points for the axisymmetric flow field from the leading edge to the 180 nose radius surface station. The results here are mainly the results for the first case of isothermal wall at $T_w^* = 800\ K$ and some initial results for the second case of adiabatic wall.

Figure 19 shows the Mach number contours of the steady state solution, where the bow shock shape is obtained as the solution for the freestream grid line. The lower figure is a blow-up of the first one near the leading edge region. The corresponding values of Mach numbers immediately behind the bow shock are shown in Fig. 20. Mach numbers approach a constant value of about 7 behind the shock at downstream locations.

Figure 21 compares steady pressure along the cone surface between the current computation and the experimental results obtained by Stetson et al [17]. There is a discontinuity in surface curvature at the junction of the sphere nose and cone afterward. The flow experiences an overexpansion at the junction and goes through a recompression along the cone surface afterward. As a result, there is a slight adverse pressure gradient at downstream surface locations. The figure shows that the surface pressure compares well with the experimental results.

Computations are currently underway to compute the steady flow solutions for the second case of adiabatic wall. Figures 22 and 23 compare the pressure and temperature distributions along the cone surface for two cases of isothermal and adiabatic walls. The results show that the pressure is not sensitive to the change of wall temperatures, while the wall temperature in the adiabatic case is lower than the first isothermal wall case.

The velocity and temperature profiles across the boundary layer at a surface location of 175 nose radius downstream are shown in Figs. 24 and 25. The linear stability analysis of the boundary layer is carried out using this steady profile. In the LST calculations, it is necessary to provide the first and second derivatives of velocity and temperature profiles in the wall-normal direction. Figures 26 and 27 show the distribution of the first and second derivatives of tangential velocities at the same surface location. In order to be consistent with the convention in LST for reference length, the nondimensional y coordinate in the wall-normal direction in these two figures is nondimensionalized by a boundary layer length scale defined by: $\delta^* = \sqrt{\frac{\nu_\infty^*}{u_\infty^* x^*}}$.

Unsteady Flow Solutions

Having obtained the steady solution, the stability of the hypersonic boundary-layer in the axisymmetric Mach 7.99 flow over the blunt cone is studied by numerical simulation. The results presented here are those for the first case of isothermal wall at $T_w^* = 800\ K$. The unsteady flow solutions are obtained by imposing surface disturbances in a narrow blowing and suction surface strip according to Eq. (34), where $\omega_0 = 9.948kHz$. The blowing and suction strip is located at about 135 nose radius downstream. The forcing wave in Eq. (34) contains seven terms of different frequencies described in Table 1. The relative nondimensional amplitudes of these amplitudes are chosen to be the same by setting A_k to 1, while their phase angles ϕ_k are randomly chosen. The dominant second mode waves observed by experiments and also predicted by the linear stability analysis is around 140 kHz. Table 1 shows that these seven forcing waves represent seven waves of equal amplitudes with amplitudes spanning a frequency range covering the frequency of the dominant second mode waves. More simulations are currently underway to include a wider range of forcing frequencies in the forcing waves.

The amplitudes of the forcing waves are determined by the parameter ϵ in Eq. (34). The nonlinear stability of the hypersonic boundary layer is studied by simulation of a number of cases with different ϵ. For the results presented in this paper, only the first case of $\epsilon = 0.0005$, which produces pressure perturbation at the blowing and suction strip at the level of approxi-

mately 3.8% of the pressure behind the shock at the same grid station. The stability is expected to be only weakly nonlinear at this forcing amplitude.

The unsteady calculations are carried out until the solutions reach a periodic state in time. Temporal Fourier analysis is carried out on local perturbations of unsteady flow variables after a time periodic state has been reached. The Fourier transform for the real disturbance functions lead to:

$$q'(x,y,t) = \Re\{\sum_{k=0}^{N} |q_k(x,y)|\, e^{i\,[-k\omega_0 t + \phi_k(x,y)]}\} \qquad (36)$$

where $k\omega_0$ is the frequency of the k-th wave mode, $q'(x,y,t)$ represents any perturbation variables, and $|q_k(x,y)|$ and $\phi_k(x,y)$ are real variables representing the local perturbation amplitude and phase angle of the k-th wave mode. These variables indicate the amplitude of local disturbances and the local phase angle with respect to the forcing waves in the freestream. For perturbations in the boundary layer near the body surface, we can define a local growth rate α_r and a local wave number α_i of the perturbation fields by,

$$\alpha_i = \frac{1}{|q_k|}\frac{d|q_k|}{dx} \qquad (37)$$

$$\alpha_r = \frac{d\phi_k}{dx} \qquad (38)$$

where the derivatives are taken along a grid line parallel to the body surface.

Figure 28 shows the distribution of the pressure perturbation amplitudes for the seven fundamental frequencies (shown in Table 1) along the body surface. The figure shows that at the end of the blowing and suction region, higher frequency waves induce higher wave amplitudes. These waves of different frequencies propagate downstream with different amplification rates, which experience nonlinear interaction among them. As shown in the figure, the wave modes of $k = 13$ and 14 are most amplified as the wave propagates downstream. The corresponding frequencies of these two modes are 129 and 139 kHz (Table 1). They are very close to the most amplified frequency observed in the experiment. The results also show that the development of these fundamental modes at low frequencies decay first, and then are followed by growth and decay afterward. This is an indication of modulation of multiple modes of the same frequency.

The total perturbations of the flow variables in the unsteady flow field is a combination of all wave modes developed in the boundary layer. Figure 29 shows the contours for the instantaneous perturbation T' after the flow field reaches a time periodic state. The instantaneous contours show the development of typical second mode instability waves in the boundary layer on the surface. The wave fields is dominated by the wave mode of the most amplified frequency at 129 and 139 kHz. As shown by Stetson's experiment, the numerical results also show that the temperature perturbations are much stronger than velocity perturbations for the second mode waves. The maximum amplitude of the temperature, as well as density, perturbations are located near the edge of the boundary layers. The shape the second-mode waves at the edge demonstrate the shape of the "rope-like" waves observed in experiments as pointed out by Stetson and Kimmel [26].

Figure 30 shows the contours for the instantaneous perturbation p'. The instantaneous profile of surface pressure perturbations in a local section of the computational domain is shown in Fig. 31. In addition to the typical second-mode wave developing in the boundary layer, there are also some acoustic waves outside of the boundary layer. These acoustic waves are induced at the blowing and suction strip and propagate along the Mach lines in the flow field. Again, the waves are dominate by the most amplified second mode waves in the boundary layer.

In response to the perturbations of the forcing waves with seven fundamental frequencies, the unsteady flow field produces second mode waves of fundamental frequencies and their harmonics. The harmonics are waves of higher frequencies created by nonlinear interactions among the fundamental modes. The frequencies of the harmonics are multiples or combinations of the fundamental frequencies. In the present case, the harmonics are mainly second order ones created by the nonlinear interactions of two fundamental modes of mode number k_1 and k_2. The frequency of the resulting harmonic by the nonlinear interaction of these two modes is

$$\omega_{k1,k2} = (k_1 + k_2)\,\omega_0 \qquad (39)$$

where the mode number for the new modes is

$$k_{k1,k2} = k_1 + k_2 \qquad (40)$$

where the self-induced second harmonics of a single fundamental k_1 mode is $k_{k1,k1} = 2k_1$ for the case of $k_1 = k_2$.

Figures 32 to 35 show the frequency spectra of surface pressure perturbation amplitudes at three surface locations downstream of the blowing and suction strip. The figures show that the wave amplitudes of the seven fundamental modes increase when the waves propagate downstream. The amplitudes of fundamental mode $k = 13$ and $k = 14$ are most amplified. At the same time, second-order harmonics also develop in strength as they propagate downstream. Figure 36 is a detailed plot of Fig. 35 to show the relative strength of the harmonics. The figure shows that the most amplified second harmonics are for a mode of

$$k = 27 = 13 + 14 \qquad (41)$$

This mode is a result of the nonlinear interaction between the two most amplified fundamental modes of

$k = 13$ and $k = 14$. The self induced second harmonic of $k = 28 = 2 * 14$ is also very strong. On the other hand, the self induced second harmonics of $k = 26 = 2 * 13$ is relatively weak. More parametric calculations are needed before detailed comparisons with experimental results can be made and conclusions can be drawn about the nonlinear interactions.

Local parallel linear stability theory (LST) is used to identify the boundary layer eigenmodes and to analyze the instability mechanisms. The LST is used to obtain instability modes based on the numerically obtained base flow between the body and the bow shock. In LST analysis, the disturbance equations are reduced to an eigenvalue problem by assuming the perturbations of flow variables in a normal mode form:

$$q' = \hat{q}(y_n)\, e^{i\,(-\omega t + \alpha\, s)} \tag{42}$$

where n and s is coordinate along the wall-normal and surface directions, α is the wave number, and $\hat{q}(y_n)$ is the eigenfunction. In the LST analysis, α and $\hat{q}(y_n)$ are obtained as the eigenvalue and eigenfunction of the stability equations for a given forcing frequency ω. For the spatial problem, ω is real, and α is a complex wave number,

$$\alpha = \alpha_r + i\ \alpha_i \tag{43}$$

where α_r and α_i represent the spatial wave number and growth rate of a wave mode respectively. The wave is unstable when α_i is negative.

The linear stability analysis can only analyze the linear fundamental wave modes in the boundary layer. The harmonics due to nonlinear interactions are neglected in the linear stability analysis. Figures 36 and 37 show the two-dimensional wave mode amplification rates as a function of frequency obtained by linear stability analysis for 2-D waves at two surface locations. The results at $x/r_n = 175$ grid station are also compared with experimental results of Stetson et al [17]. The LST results in the first mode region is most unstable when they are three-dimensional waves. In the current calculation, both first and second modes are the two-dimensional wave modes only. The resulting first mode is lower than LST results reported by other researchers [18–21]. The figures show that the most amplified waves are second mode waves with a fundamental frequency near 140 kHz. As the wave propagates downstream, the most amplified frequency moves to a lower frequency. The LST results over predict experimental values on the amplification rates, but the frequency is very close to the experimental results.

The identification of the wave modes computed by the numerical simulations is further examined by comparing the LST eigenfunctions with Fourier amplitudes of the Navier-Stokes solutions at the same fundamental frequency. For the purpose of comparison, the eigenfunctions are normalized by their respective pressure perturbation at the wall. Figures 38 and 39 show the comparison of the normalized temperature and velocity amplitudes along grid lines normal to the parabola surface at a surface location of 160 nose radius for the wave frequency 139.27 kHz ($k = 14$). The figure shows that numerical solutions agree reasonably well with the LST second mode. As stated earlier in this paper, the figures also show that the relative temperature perturbation amplitudes in hypersonic boundary layer is about 40 times stronger than those of the velocity perturbations. The peak of the temperature of the second mode wave are at the edge of the boundary layer, which is responsible for producing the "rope-like" shaped wave in hypersonic boundary layers.

CONCLUSIONS

This paper has presented new high-order (12th or higher order) finite difference schemes with stable boundary closures for the DNS of transitional or turbulent flows. In addition, numerical studies have been conducted on the stability of Mach 7.99 flow over a blunt cone. The emphasis is on the nonlinear second mode instability of the boundary layer observed in Stetson's experiment. The initial results of the first test case have been finished and they have been presented in the paper. The conclusions are:

1. We have argued and shown that high-order finite difference schemes with high-order boundary closure schemes of the same order can be made stable when they are derived based on a stretched grid in the physical domain, instead of a uniform computational domain. We have also developed explicit formulas for computing the coefficients of high-order compact (and explicit) schemes on nonuniform grids. The high-order schemes on nonuniform grids can be easily applied in practical calculations by computing once and for all of the derivative (banded) matrix at the beginning of a calculation.

2. A requirement of grid stretching to meet the stability requirement for high-order schemes with boundary closure has been established by asymptotic stability analysis. For the explicit scheme, arbitrarily high-order schemes can be made stable by grid stretching. It is shown that the minimum grid stretching for a fixed arbitrary high-order explicit finite difference scheme is proportional to $1/N$, which is much less restrictive than spectral collocation schemes. On the other hand, the compact scheme of 12th or higher order cannot be made stable by grid stretching.

3. The new high-order schemes have been tested in wave equations of up to 16th order. It has been found that the accuracy can be increased sufficiently when the order of schemes is increased to 10th-order or higher. Such implementations are

much more efficient than a spectral collocations method in terms of spectral derivative and in terms of time step restrictions. Work is underway to extend the schemes to full Navier-Stokes equations.

4. We have finished the computation of one case of Mach 7.99 flow over a cone with an isothermal wall. The steady surface pressure compared well with experimental values.

5. We have done one case of stability calculations with seven frequencies component in the forcing waves in surface blowing and suction. Other unstable cases are currently under calculation. The results of the present case show that the wave modes develop into second-mode waves downstream. The dominant waves are frequency agree well with experimental results. The eigenfunction of the modes obtained by the numerical simulations also agree very well with the LST results. The numerical results also show the development of second harmonics due to the nonlinear interaction among these fundamental waves. This is a case with very weak nonlinear effects due to relative weak initial forcing waves. A stronger forcing waves case is currently being computed to study the nonlinear effects in more detail and will be compared with experimental results.

ACKNOWLEDGMENTS

This research was supported by the Air Force Office of Scientific Research under grant number F49620-00-1-0101 monitored by Dr. Robert Herklotz.

References

[1] Mack, L. M., "Boundary Layer Linear Stability Theory," *AGARD report, No. 709*, 1984, pp. 3–1 to 3–81.

[2] Arnal, D., "Laminar-Turbulent Transition Problems In Supersonic and Hypersonic Flows," *Special Course on Aerothermodynamics of Hypersonic Vehicles*, Vol. AGARD Report No. 761, 1988.

[3] Stetson, K. F. and Kimmel, R. L., "On Hypersonic Boundary Layer Stability," *AIAA paper 92-0737*, 1992.

[4] Zhong, X., "Direct Numerical Simulation of Hypersonic Boundary-Layer Transition Over Blunt Leading Edges, Part I: New Numerical Methods and Validation (Invited)," *AIAA paper 97-0755, 35th AIAA Aerospace Sciences Meeting and Exhibit, January 6-9, Reno, Nevada*, 1997.

[5] Zhong, X., "High-Order Finite-Difference Schemes for Numerical Simulation of Hypersonic Boundary-Layer Transition," *Journal of Computational Physics*, Vol. 144, August 1998, pp. 662–709.

[6] Lele, S. K., "Compact Finite Difference Schemes with Spectral-like Resolution," *Journal of Computational Physics*, Vol. 103, 1992, pp. 16–42.

[7] Pruett, C. D., Zang, T. A., Chang, C.-L., and Carpenter, M. H., "Spatial Direct Numerical Simulation of High-Speed Boundary-Layer Flows, Part I: Algorithmic Considerations and Validation," *Theoretical and Computational Fluid Dynamics*, Vol. 7, 1995, pp. 49–76.

[8] Adams, N. A., "Subharmonic Transition to Turbulence in a Flat-Plate Boundary Layer at Mach Number 4.5," *Journal of Fluid Mechanics*, Vol. 317, 1996, pp. 301–335.

[9] Mahesh, K., "A Family of High Order Finite Difference Schemes with Good Spectral Resolution," *Journal of Computational Physics*, Vol. Vol. 145, pp. 332–358, 1998.

[10] Gaitonde, D. V. and Visbal, M. R., "Further Development of a Navier-Stokes Solution Procedure Based on Higher-Order Formulas," *AIAA paper 99-0557*, 1999.

[11] Rai, M. M. and Moin, P., "Direct Numerical Simulation of Transition and Turbulence in a Spatially Evolving Boundary Layer," *Journal of Computational Physics*, Vol. 109, 1993, pp. 169–192.

[12] Zingg, D. W., Lomax, H., and Jurgens, H., "High-Accuracy Finite-Difference Schemes for Linear Wave Propagation," *SIAM Journal of Scientific Comput.*, Vol. 17, No. 2, 1995, pp. 328–346.

[13] Adams, N. A. and Shariff, K., "A High-Resolution Hybrid Compact-ENO Scheme for Shock-Turbulence Interaction Problems," *Journal of Computational Physics*, Vol. 127, 1996, pp. 27–51.

[14] Carpenter, M. H., Gotlieb, D., and Abarbanel, S., "The Stability of Numerical Boundary Treatments for Compact High-Order Finite-Difference Schemes," *Journal of Computational Physics*, Vol. 108, 1993, pp. 272–295.

[15] Abarbanel, S. S., Chertock, A. E., and Yefet, A., "Strict Stability of High-Order Compact Implicit Finite-Difference Schemes: The Role of Boundary Conditions for Hyperbolic PDEs,I," *Journal of Computational Physics*, Vol. Vol. 160, pp. 42–66, 2000.

[16] Schneider, S. P., "Hypersonic Laminar Instability on Round Cones Near Zero Angle of Attack," *AIAA Paper 2001-0206*, 2001.

[17] Stetson, K. F., Thompson, E. R., Donaldson, J. C., and Siler, L. G., "Laminar Boundary Layer Stability Experiments on a Cone at Mach 8, Part 2: Blunt Cone," *AIAA paper 84-0006*, January 1984.

[18] Malik, M. R., Spall, R. E., and Chang, C.-L., "Effect of Nose Bluntness on Boundary Layer Stability and Transition," *AIAA paper 90-0112*, 1990.

[19] Herbert, T. and Esfahanian, V., "Stability of Hypersonic Flow over a Blunt Body," *AGARD CP-514*, Vol. pp. 28-1 – 12, April, 1993.

[20] Kufner, E., Dallmann, U., and Stilla, J., "Instability of Hypersonic Flow Past Blunt Cones – Effects of Mean Flow Variations," *AIAA paper 93-2983*, June 1993.

[21] Kufner, E. and Dallmann, U., "Entropy- and Boundary Layer Instability of Hypersonic Cone Flows – Effects of Mean Flow Variations," *IUTAM Symposium on Laminar-Turbulent Transition*, Vol. Sendai/Japan, September 1994, pp. 197-204, Springer-Verlag, Berlin, 1994.

[22] Reshotko, E., "Hypersonic Stability and Transition," *in Hypersonic Flows for Reentry Problems, Eds. J.-A. Desideri, R. Glowinski, and J. Periaux, Springer-Verlag*, Vol. 1, 1991, pp. 18–34.

[23] Morkovin, M. V., "Transition at Hypersonic Speeds," *ICASE Interim Report 1*, Vol. NASA CR 178315, May, 1987.

[24] Kosloff, D. and Tal-Ezer, H., "A Modified Chebyshev Pseudospectral Method with an O(1/N) Time Step Restriction," *Journal of Computational Physics*, Vol. Vol. 104, pp. 457–469, 1993.

[25] Zhong, X., "Direct Numerical Simulation of Hypersonic Boundary-Layer Transition Over Blunt Leading Edges, Part II: Receptivity to Sound (Invited)," *AIAA paper 97-0756*, January 1997.

[26] Stetson, K. F. and Kimmel, R., "On the Breakdown of a Hypersonic Laminar Boundary Layer," *AIAA Paper 93-0896*, 1993.

Table 2: **Average error (L-1 norm) for explicit high order scheme solutions of the wave equation.**

	21 Pts	41 Pts	51 Pts	101 Pts
2nd order	0.326162889E-01	0.810332811E-02	0.518681321E-02	0.129591602E-02
4th order	0.843494315E-03	0.551459581E-04	0.227042686E-04	0.142848006E-05
6th order	0.243947839E-04	0.413791452E-06	0.109559034E-06	0.173423464E-08
8th order	0.718268037E-06	0.325263739E-08	0.555259542E-09	0.221586820E-11
10th order	0.215320258E-07	0.263122100E-10	0.289553460E-11	0.292310374E-14
12th order	0.610218527E-09	0.215510847E-12	0.153853384E-13	0.402305767E-17

Appendix A

The spatial discretization using an explicit scheme can be written in the matrix form given by Eq. (9). An example of derivative $\boldsymbol{A}$ in Eq. (9) for a 15 point domain (with $\alpha = 0.91$) and a 6th order scheme using seven grid stencil in both interior and in boundary points is given in the matrix below. The numbers below are truncated to three significants as a demonstration, the actual significant digits of the coefficients are longer with about 15 digits for double precision calculations and can be longer if necessary.

$$A = \begin{bmatrix}
-36.368 & 45.503 & -12.961 & 5.316 & -1.887 & 0.448 & -0.051 & \cdot & \cdot & \cdot & \cdot & \cdot & \cdot & \cdot & \cdot & 0 \\
-10.592 & 4.043 & 8.758 & -3.011 & 1.008 & -0.233 & 0.026 & & & & & & & & & \cdot \\
3.042 & -8.831 & 1.570 & 5.340 & -1.379 & 0.288 & -0.030 & & & & & & & & & \cdot \\
-1.988 & 4.836 & -8.508 & 2.824 & 3.309 & -0.524 & 0.050 & & & & & & & & & \cdot \\
\cdot & -0.291 & 1.566 & -5.532 & 1.062 & 3.812 & -0.689 & 0.071 & & & & & & & & \cdot \\
\cdot & & -0.152 & 1.099 & -4.731 & 0.462 & 4.008 & -0.769 & 0.083 & & & & & & & \cdot \\
\cdot & & & -0.116 & 0.943 & -4.403 & 0.183 & 4.121 & -0.819 & 0.092 & & & & & & \cdot \\
\cdot & & & & -0.101 & 0.869 & -4.233 & 0.000 & 4.233 & -0.869 & 0.101 & & & & & \cdot \\
\cdot & & & & & -0.092 & 0.819 & -4.121 & -0.183 & 4.403 & -0.943 & 0.116 & & & & \cdot \\
\cdot & & & & & & -0.083 & 0.769 & -4.008 & -0.462 & 4.731 & -1.099 & 0.152 & & & \cdot \\
\cdot & & & & & & & -0.071 & 0.689 & -3.812 & -1.062 & 5.532 & -1.566 & 0.291 & & \cdot \\
\cdot & & & & & & & & -0.050 & 0.524 & -3.309 & -2.824 & 8.508 & -4.836 & 1.988 & \\
\cdot & & & & & & & & 0.030 & -0.288 & 1.379 & -5.340 & -1.570 & 8.831 & -3.042 & \\
\cdot & & & & & & & & -0.026 & 0.233 & -1.008 & 3.011 & -8.758 & -4.043 & 10.592 & \\
0 & \cdot & \cdot & \cdot & \cdot & \cdot & \cdot & \cdot & 0.051 & -0.448 & 1.887 & -5.316 & 12.961 & -45.503 & 36.368 &
\end{bmatrix} \tag{44}$$

The spatial discretization using a compact scheme can be written in matrix form given by Eq. (25). An example of the coefficient matrices $\boldsymbol{P}$ and $\boldsymbol{Q}$ for a 7-3 compact scheme for a 15 point domain (with $\alpha = 0.8$) is given below:

$$P = \begin{bmatrix}
1.000 & 0.223 & -0.066 & \cdot & \cdot & \cdot & \cdot & \cdot & \cdot & \cdot & \cdot & \cdot & \cdot & \cdot & 0 \\
0.046 & 1.000 & 0.343 & & & & & & & & & & & & \cdot \\
\cdot & 0.615 & 1.000 & 0.340 & & & & & & & & & & & \cdot \\
\cdot & & 0.791 & 1.000 & 0.251 & & & & & & & & & & \cdot \\
\cdot & & & 0.519 & 1.000 & 0.306 & & & & & & & & & \cdot \\
\cdot & & & & 0.439 & 1.000 & 0.339 & & & & & & & & \cdot \\
\cdot & & & & & 0.402 & 1.000 & 0.361 & 0.380 & & & & & & \cdot \\
\cdot & & & & & & 0.380 & 1.000 & 1.000 & 0.402 & & & & & \cdot \\
\cdot & & & & & & & 0.361 & 0.339 & 1.000 & 0.439 & & & & \cdot \\
\cdot & & & & & & & & & 0.306 & 1.000 & 0.519 & & & \cdot \\
\cdot & & & & & & & & & & 0.251 & 1.000 & 0.791 & & \cdot \\
\cdot & & & & & & & & & & & 0.340 & 1.000 & 0.615 & \cdot \\
\cdot & & & & & & & & & & & & 0.343 & 1.000 & 0.046 \\
0 & \cdot & \cdot & \cdot & \cdot & \cdot & \cdot & \cdot & \cdot & \cdot & \cdot & \cdot & -0.066 & 0.223 & 1.000
\end{bmatrix} \tag{45}$$

$$Q = \begin{bmatrix}
-44.750 & 49.766 & -5.503 & 0.524 & -0.040 & 0.004 & -0.0002 & \cdot & \cdot & \cdot & \cdot & \cdot & \cdot & \cdot & \cdot & 0 \\
-16.392 & 8.256 & 7.948 & 0.203 & -0.016 & 0.001 & -0.0001 & & & & & & & & & \cdot \\
-6.887 & -2.559 & 3.923 & 5.335 & 0.199 & -0.012 & 0.0005 & & & & & & & & & \cdot \\
1.469 & -4.748 & -4.831 & 4.308 & 3.705 & 0.100 & -0.003 & & & & & & & & & \cdot \\
\cdot & 0.104 & -0.949 & -4.972 & 1.804 & 3.857 & 0.162 & -0.006 & & & & & & & & \cdot \\
\cdot & & 0.034 & -0.491 & -4.483 & 0.837 & 3.906 & 0.206 & -0.008 & & & & & & & \cdot \\
\cdot & & & 0.019 & -0.349 & -4.196 & 0.341 & 3.952 & 0.243 & -0.010 & & & & & & \cdot \\
\cdot & & & & 0.013 & -0.284 & -4.037 & 0.000 & 4.037 & 0.284 & -0.013 & & & & & \cdot \\
\cdot & & & & & 0.010 & -0.243 & -3.952 & -0.341 & 4.196 & 0.349 & -0.019 & & & & \cdot \\
\cdot & & & & & & 0.008 & -0.206 & -3.906 & -0.837 & 4.483 & 0.491 & -0.034 & & & \cdot \\
\cdot & & & & & & & 0.006 & -0.162 & -3.857 & -1.804 & 4.972 & 0.949 & -0.104 & & \cdot \\
\cdot & & & & & & & & 0.003 & -0.100 & -3.705 & -4.308 & 4.831 & 4.748 & -1.469 & \\
\cdot & & & & & & & & -0.0005 & 0.012 & -0.199 & -5.335 & -3.923 & 2.559 & 6.887 & \\
\cdot & & & & & & & & 0.0001 & -0.001 & 0.016 & -0.203 & -7.948 & -8.256 & 16.392 & \\
0 & \cdot & \cdot & \cdot & \cdot & \cdot & \cdot & \cdot & 0.0002 & -0.004 & 0.040 & -0.524 & 5.503 & -49.766 & 44.750 &
\end{bmatrix} \tag{46}$$

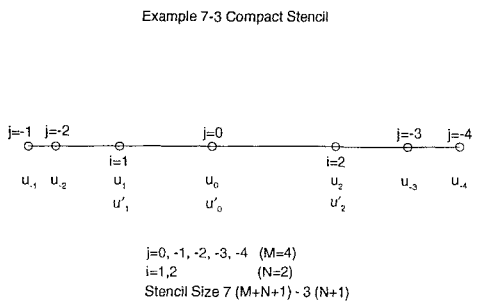

Figure 1: A 7-3 compact scheme stencil on a nonuniform grid.

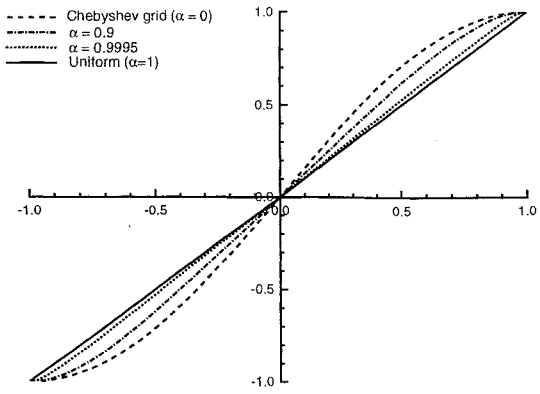

Figure 2: Grid stretching function used in this paper (x vs. i/N).

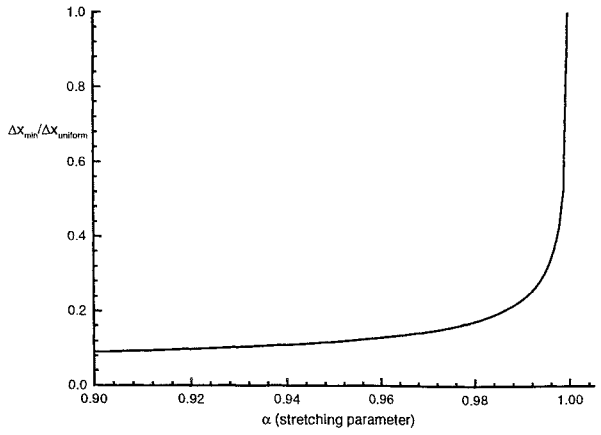

Figure 3: Grid stretching factor as a function of the stretching parameter α.

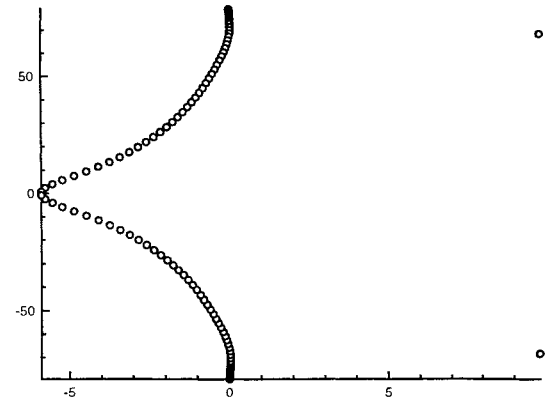

Figure 4: Eigenvalue spectrum of the spatial discretization matrix for the 6th order scheme on a uniform grid of 101 points.

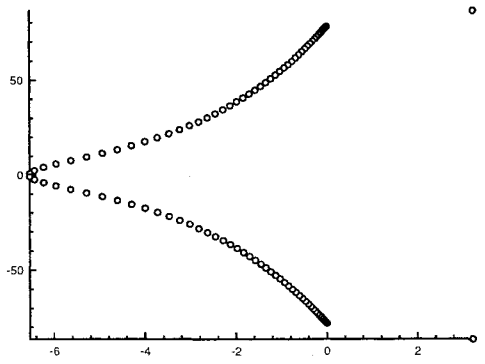

Figure 5: Eigenvalue spectrum of the spatial discretization matrix for the 6th order scheme on a stretched grid of 101 points with $\alpha = 0.9997$.

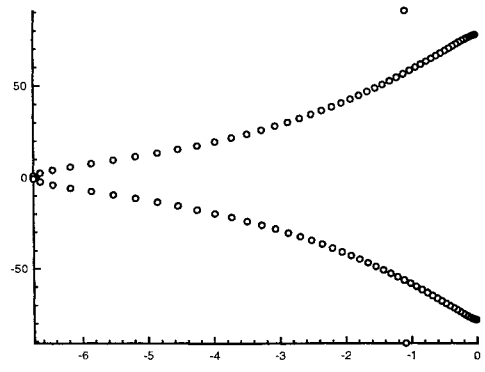

Figure 6: Eigenvalue spectrum of the spatial discretization matrix for the 6th order scheme on a stretched grid of 101 points with $\alpha = 0.9995$.

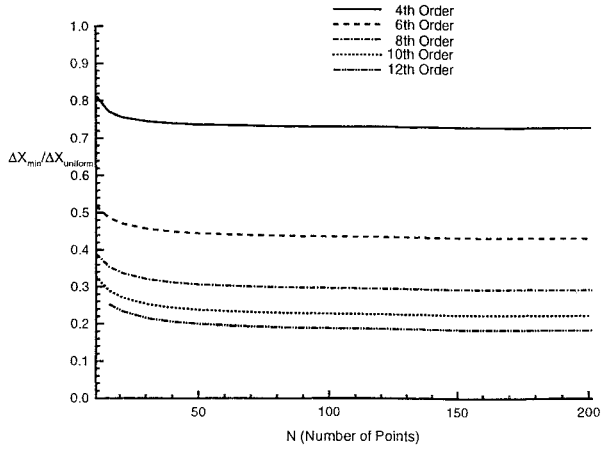

Figure 7: Variation of minimum Δx required for stable boundary closure with the total points used, for various schemes.

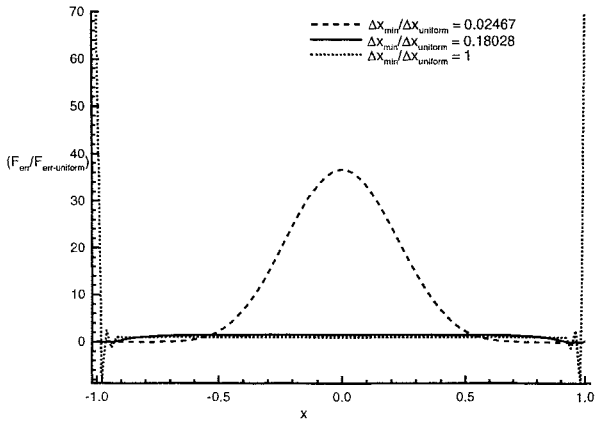

Figure 10: Distribution of the truncation error (normalized by the maximum uniform grid truncation error) for a sixth order scheme for 101 points.

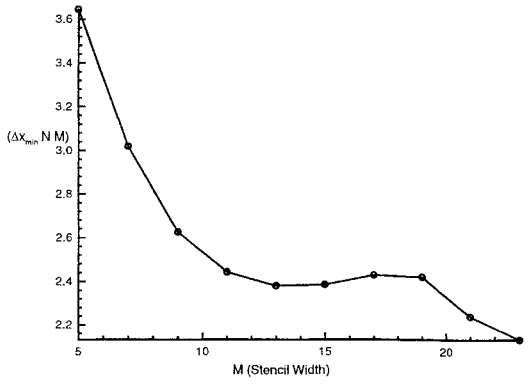

Figure 8: Variation of minimum Δx required for stable boundary closure with the stencil width, for various schemes.

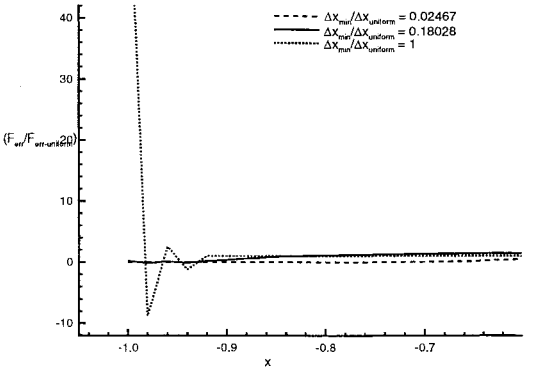

Figure 11: Distribution of the truncation error (normalized by the maximum uniform grid truncation error) for a sixth order scheme for 101 points.

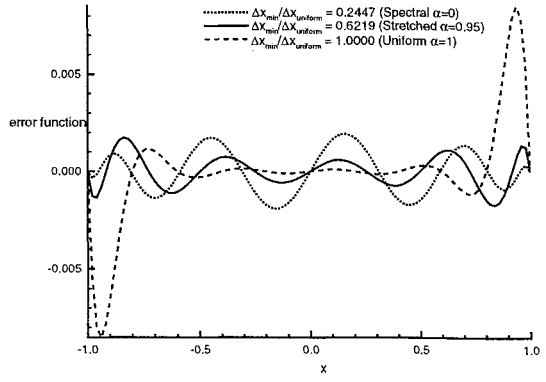

Figure 9: Distribution of the truncation error for a 11 points global scheme with different grid spacing.

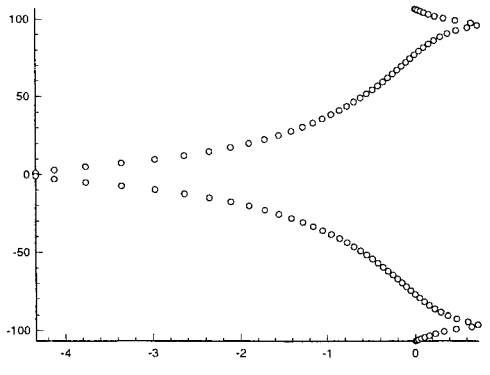

Figure 12: Eigenvalue spectrum of the spatial discretization matrix for the $7-3$ compact scheme on a uniform grid of 101 points.

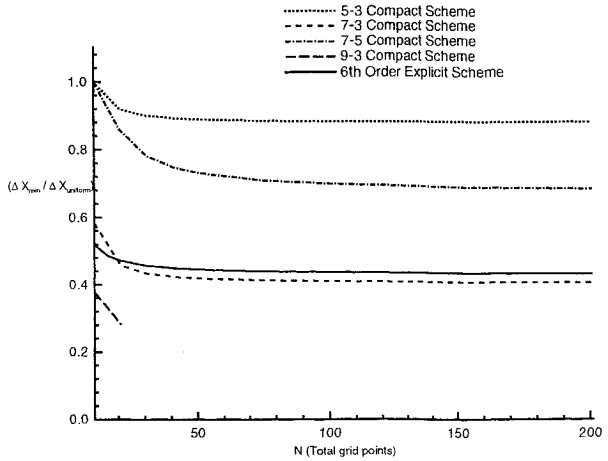

Figure 13: Variation of minimum Δx required for stable boundary closure with the stencil width, for various compact schemes.

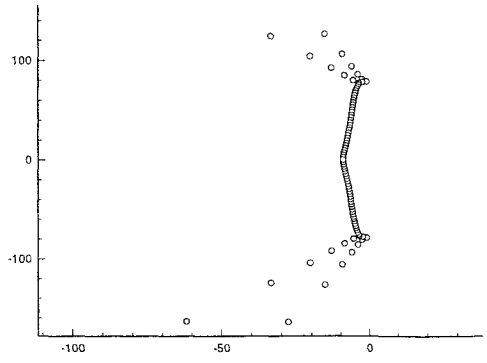

Figure 14: Eigenvalue spectrum of the spatial discretization matrix for the $7-3$ compact scheme on a stretched grid of 101 points with $\alpha = 0.8$.

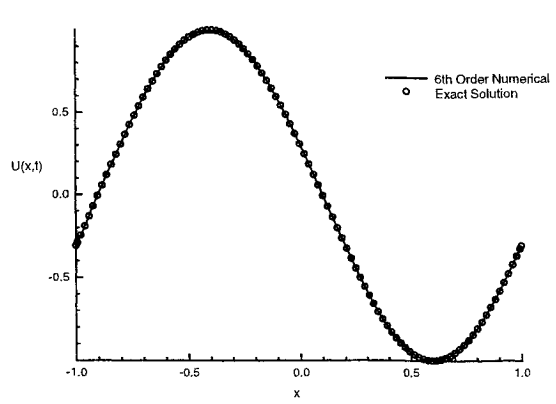

Figure 15: Comparison of numerical solution, using a 6th order explicit scheme on a stretched grid ($\alpha = 0.91$), with the exact solution at $t = 1$ seconds.

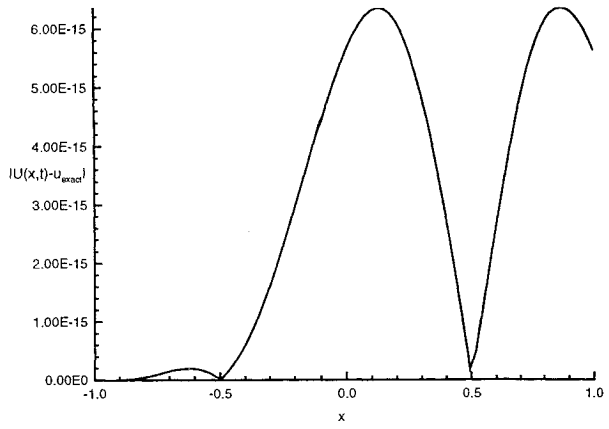

Figure 16: Error distribution for numerical solution, using a 10th order explicit scheme on a stretched grid ($\alpha = 0.91$), at $t = 1$ second.

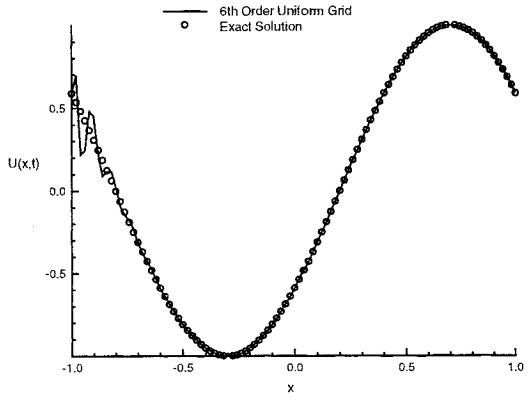

Figure 17: Comparison of numerical solution , using a 6th order explicit scheme on an uniform grid, with the exact solution at $t = 2.2$ seconds.

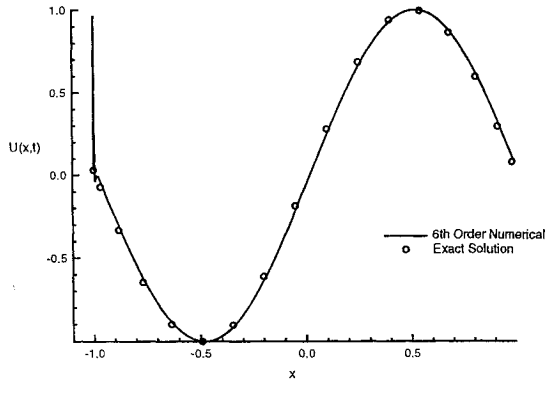

Figure 18: Comparison of numerical solution (at $t = 0.01s$) using a stretched grid and is computed by a 6th order explicit scheme on a uniform grid through coordinate transformation.

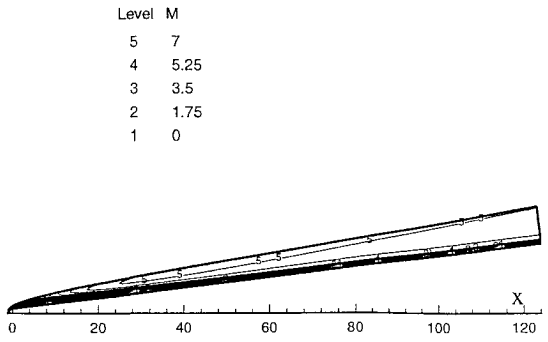

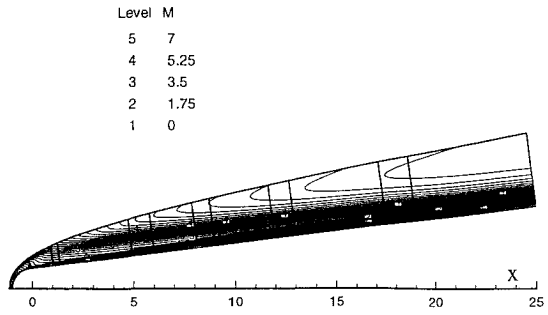

Figure 19: Multi-zone solutions of Mach number contours for steady Mach 7.99 flow over a 7 degree half angle round blunt cone at the same flow conditions as Stetson's experiments (1984), and an isothermal wall.

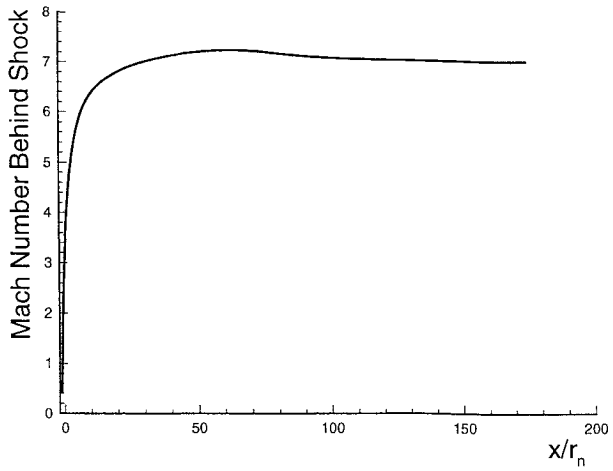

Figure 20: Steady Mach number immediately behind the bow shock vs. x.

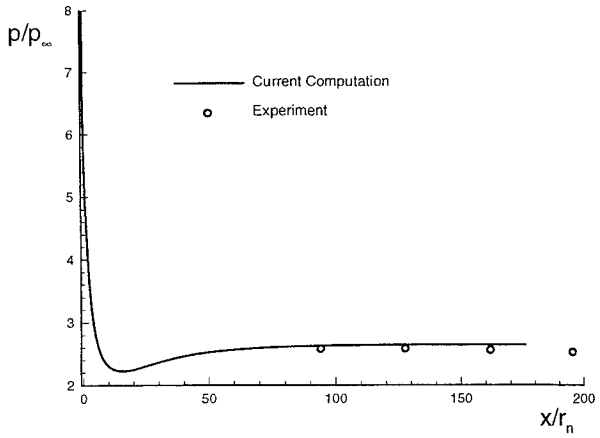

Figure 21: Steady pressure along the cone surface. The experimental results were obtained by Stetson et al. (1984).

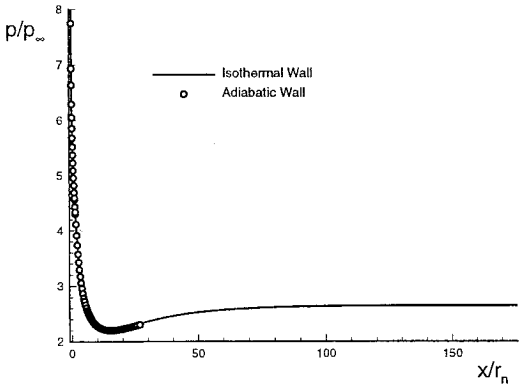

Figure 22: Comparison of steady pressure distributions along the cone surface for two cases of isothermal and adiabatic walls.

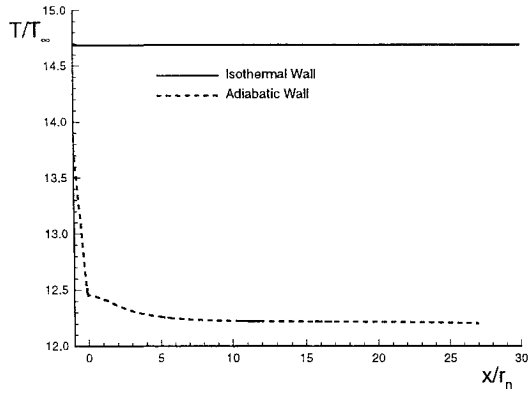

Figure 23: Comparison of steady temperature distributions along the cone surface for two cases of isothermal and adiabatic walls.

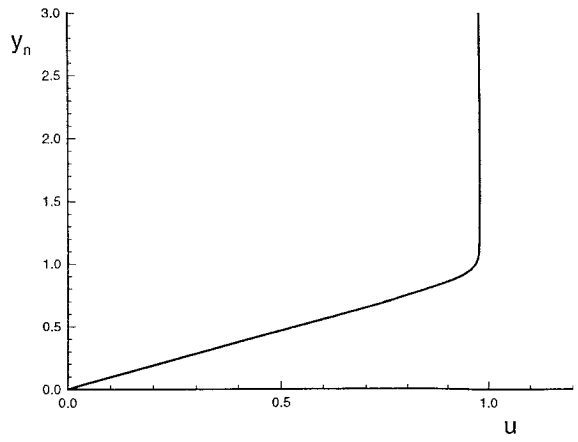

Figure 24: Steady tangential velocity profile along the wall-normal direction at the surface location of 175 nose radius.

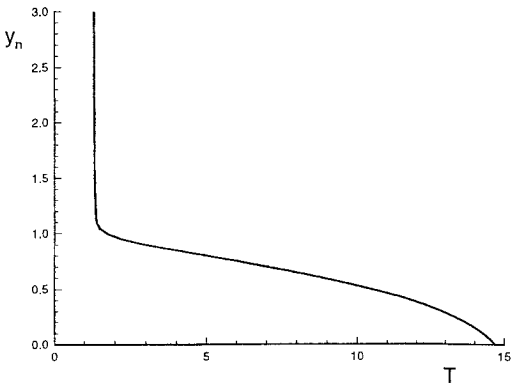

Figure 25: Steady temperature profile along the wall-normal direction at the surface location of 175 nose radius.

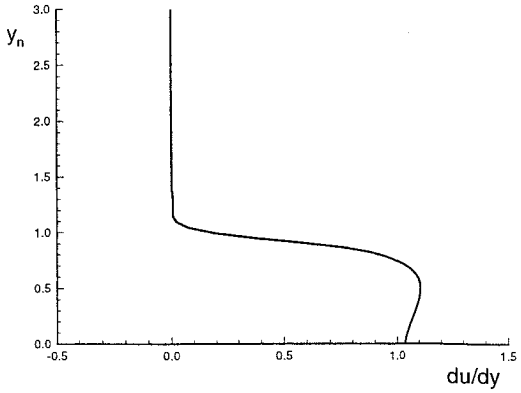

Figure 26: First derivative of tangential velocity along the wall-normal direction at the surface location of 175 nose radius.

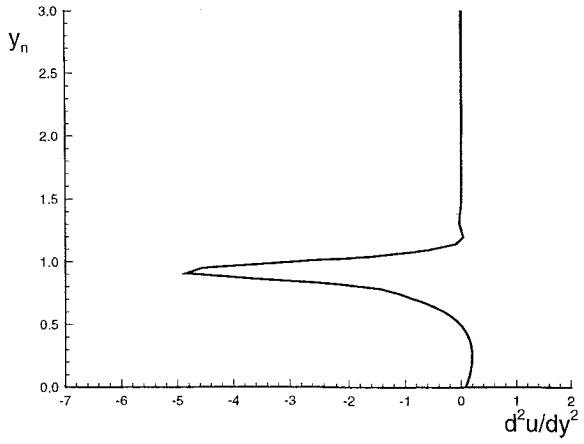

Figure 27: Second derivative of tangential velocity along the wall-normal direction at the surface location of 175 nose radius.

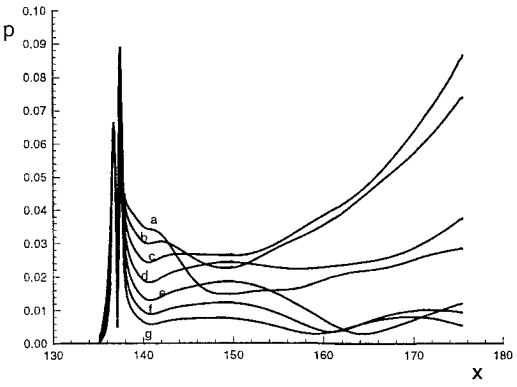

Figure 28: Amplitudes of pressure perturbations for the seven fundamental frequencies along the body surface. The labels "a" to "g" refer to kth wave modes of different frequency for k changing from 15 to 9, respectively.

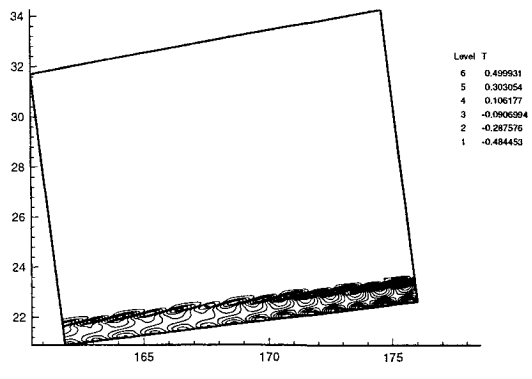

Figure 29: Instantaneous contours of temperature perturbations in a local section of the computational domain.

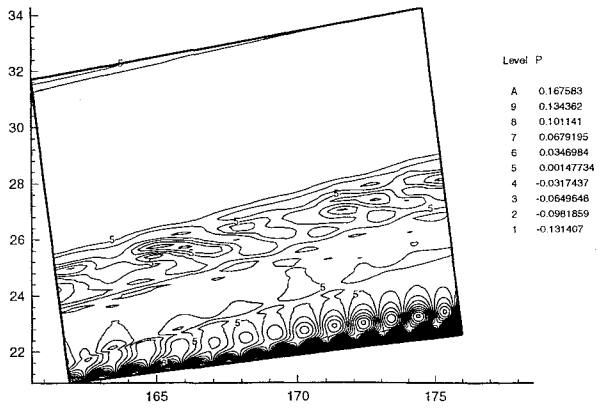

Figure 30: Instantaneous contours of pressure perturbations in a local section of the computational domain.

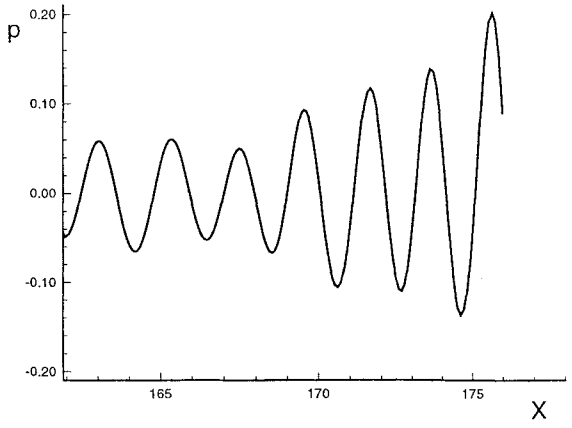

Figure 31: Instantaneous profile of surface pressure perturbations in a local section of the computational domain.

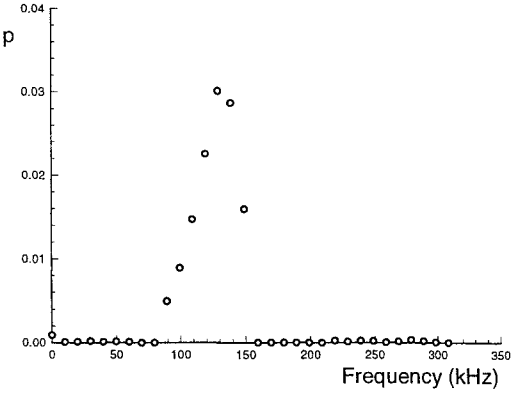

Figure 32: Frequency spectra of surface pressure perturbation amplitudes at surface location of 155 nose radius from the leading edge.

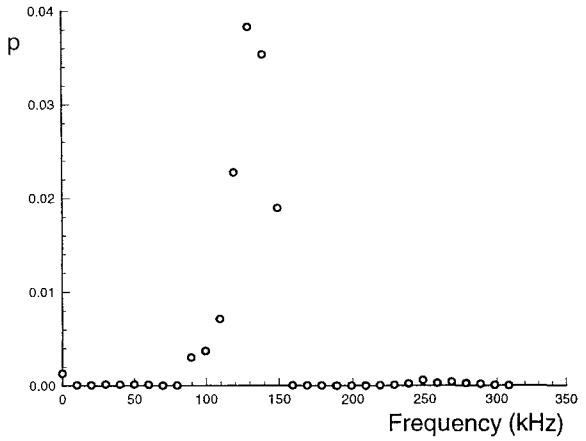

Figure 33: Frequency spectra of surface pressure perturbation amplitudes at surface location of 160 nose radius from the leading edge.

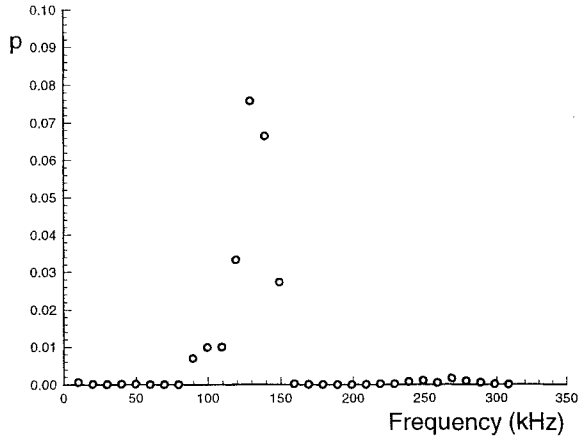

Figure 34: Frequency spectra of surface pressure perturbation amplitudes at surface location of 175 nose radius from the leading edge.

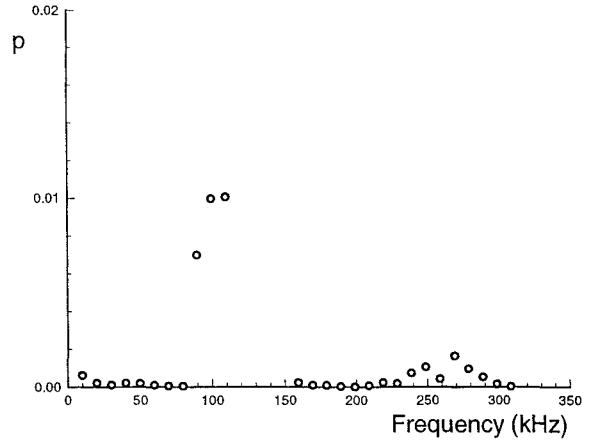

Figure 35: Blow-up plot of the previous figure.

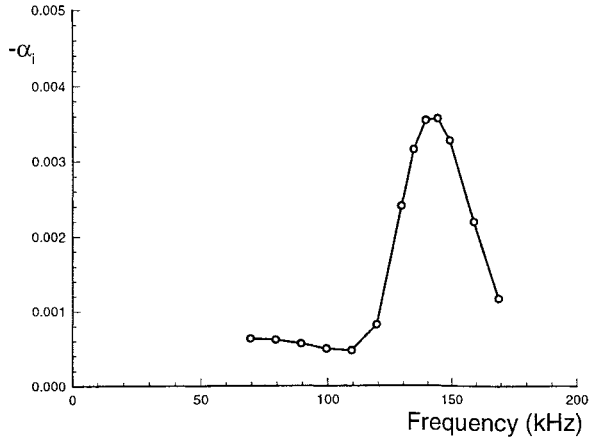

Figure 36: Two-dimensional wave mode amplification rates as a function of frequency obtained by linear stability analysis for 2-D waves at the $x/r_n = 160$ surface location.

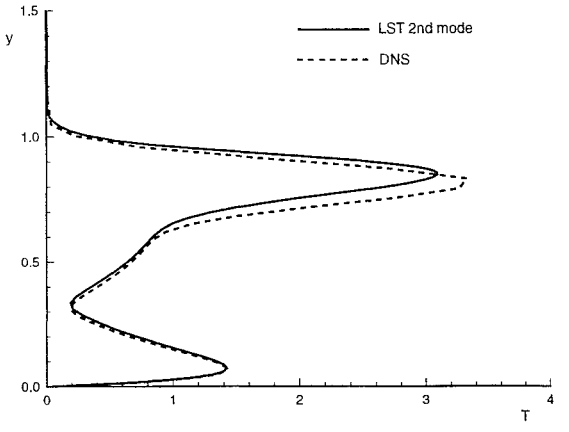

Figure 38: Temperature perturbation amplitudes distribution in the wall-normal direction at $x/r_n = 160$ nose radius surface location for wave frequency 139.27 kHz ($k = 14$).

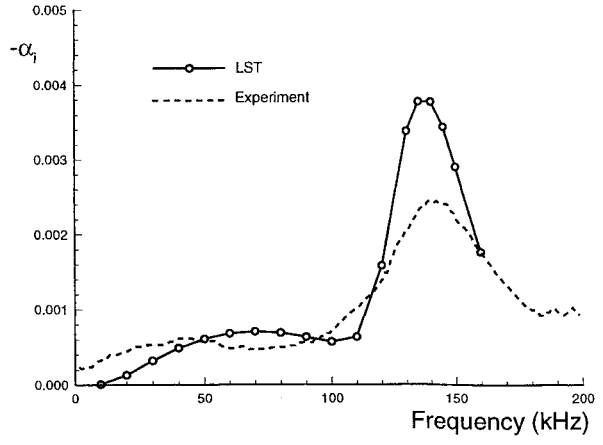

Figure 37: Two-dimensional wave mode amplification rates as a function of frequency obtained by linear stability analysis for 2-D waves at the $x/r_n = 175$ surface location. The experimental results were obtained by Stetson et al. (1984).

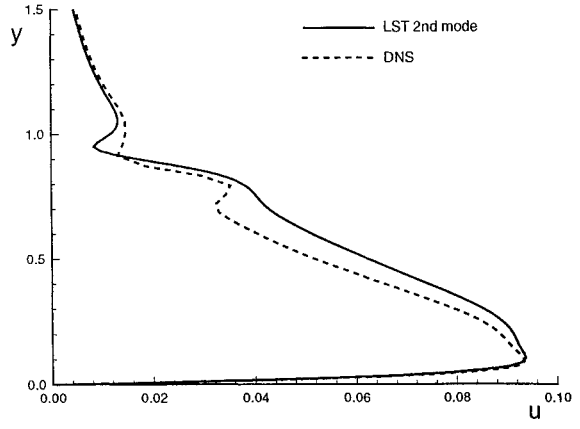

Figure 39: Tangential velocity perturbation amplitudes distribution in the wall-normal direction at $x/r_n = 160$ nose radius surface location for wave frequency 139.27 kHz ($k = 14$).